



Politecnico di Bari

Repository Istituzionale dei Prodotti della Ricerca del Politecnico di Bari

Meeting the Contact-Mechanics Challenge

This is a post print of the following article

Original Citation:

Meeting the Contact-Mechanics Challenge / Mueser, Martin H.; Dapp, Wolf B.; Bugnicourt, Romain; Sainsot, Philippe; Lesaffre, Nicolas; Lubrecht, Ton A.; Persson, Bo N. J.; Harris, Kathryn; Bennett, Alexander; Schulze, Kyle; Rohde, Sean; Ifju, Peter; Sawyer, W. Gregory; Angelini, Thomas; Ashtari Esfahani, Hossein; Kadkhodaei, Mahmoud; Akbarzadeh, Saleh; Jiunn jong, Wu; Vorlaufer, Georg; Vernes, Andr  s; Solhjoo, Soheil; Vakis, Antonis I.; Jackson, Robert L.; Yang, Xu; Streater, Jeffrey; Rostami, Amir; Dini, Daniele; Medina, Simon; Carbone, Giuseppe; Bottiglione, Francesco; Afferrante, Luciano; Monti, Joseph; Pastewka, Lars; Robbins, Mark O.; Greenwood, James A.. - In: TRIBOLOGY LETTERS. - ISSN 1023-8883. - STAMPA. - 65:4(2017). [10.1007/s11249-017-0900-2]
This version is available at <http://hdl.handle.net/11589/117004> since: 2022-06-22

Published version

DOI:10.1007/s11249-017-0900-2

Terms of use:

(Article begins on next page)

Meeting the contact-mechanics challenge

Martin H. Müser · Wolf B. Dapp · Romain Bugnicourt · Philippe Sainsot · Nicolas Lesaffre · Ton A. Lubrecht · Bo N. J. Persson · Kathryn Harris · Alexander Bennett · Kyle Schulze · Sean Rohde · Peter Ifju · W. Gregory Sawyer · Thomas Angelini · Hossein Ashtari Esfahani · Mahmoud Kadkhodaei · Saleh Akbarzadeh · Jiunn-Jong Wu · Georg Vorlaufer · András Vernes · Soheil Solhjoo · Antonis I. Vakis · Robert L. Jackson · Yang Xu · Jeffrey Streater · Amir Rostami · Daniele Dini · Simon Medina · Giuseppe Carbone · Francesco Bottiglione · Luciano Afferrante · Joseph Monti · Lars Pastewka · Mark O. Robbins · James A. Greenwood

Received: date / Accepted: date

M. H. Müser

Department of Materials Science and Engineering, Saarland University, Campus, 66123 Saarbrücken, Germany E-mail: martin.mueser@mx.uni-saarland.de

M. H. Müser · W. B. Dapp

John von Neumann Institut für Computing and Jülich Supercomputing Centre, Institute for Advanced Simulation, FZ Jülich, 52425 Jülich, Germany

R. Bugnicourt · P. Sainsot · N. Lesaffre · T. A. Lubrecht

Université Lyon, INSA-Lyon, CNRS UMR5259, Laboratoire de Mécanique des Contacts et des Structures, 69621 Villeurbanne - Cedex, France

R. Bugnicourt

Manufacture Française des Pneumatiques Michelin, Centre de Technologie de Ladoux, 63118 Cébazat, France

Bo N. J. Persson

PGI-1, FZ-Jülich, 52425 Jülich, Germany

Kathryn Harris · Alexander Bennett · Kyle Schulze · Sean Rohde · Peter Ifju · W. Gregory Sawyer · Thomas Angelini

Department of Mechanical & Aerospace Engineering, University of Florida, Gainesville, FL 32611, USA

Hossein Ashtari Esfahani · Mahmoud Kadkhodaei · Saleh Akbarzadeh

Department of Mechanical Engineering, Isfahan University of Technology, Isfahan 84156-83111, Iran

Jiunn-Jong Wu

Department of Mechanical Engineering, Chang Gung University, Taoyuan City, Taiwan

Georg Vorlaufer · András Vernes

AC2T research GmbH, Viktor-Kaplan-Straße 2/C, 2700 Wiener Neustadt, Austria

Soheil Solhjoo · Antonis I. Vakis

Advanced Production Engineering, Engineering and Technology Institute Groningen, Faculty of Science and Engineering, University of Groningen, 9747 AG Groningen, the Netherlands

Abstract This paper summarizes the submissions to a recently announced contact-mechanics modeling challenge. The task was to solve a typical, albeit mathematically fully defined, contact-mechanics problem. The surface topography of the rough, rigid substrate, the elastic properties of the indenter, as well as the short-range adhesion between indenter and substrate were specified so that diverse quantities of interest, e.g., the distribution of interfacial stresses at a given load or the mean gap as a function of load, could be computed and compared to a reference solution. Many different solution strategies were pursued, ranging from traditional asperity-based

Robert L. Jackson · Yang Xu

Auburn University, Auburn, AL 36849, USA

Jeffrey Streater · Amir Rostami

Georgia Institute of Technology, Atlanta, GA 30332, USA

Daniele Dini · Simon Medina

Department of Mechanical Engineering, Imperial College London, London SW7 2AZ, UK

Giuseppe Carbone · Francesco Bottiglione · Luciano Afferrante

Department of Mechanics, Mathematics and Management, Polytechnic University of Bari, 70126 Bari, Italy

Joseph Monti · Mark O. Robbins

Department of Physics & Astronomy, Johns Hopkins University, Baltimore, MD 21218, USA

Lars Pastewka

Department of Microsystems Engineering, University of Freiburg, Germany

Institute for Applied Materials (IAM), Karlsruhe Institute of Technology (KIT), 76131 Karlsruhe, Germany

James A. Greenwood

Department of Engineering, University of Cambridge, Cambridge CB2 1PZ, UK

models via Persson theory and brute-force computational approaches, to real-laboratory experiments and all-atom molecular dynamics simulations of a model, in which the original assignment was scaled down to the atomistic scale. While each submission contained satisfying answers for at least a subset of the posed questions, efficiency, versatility, and accuracy differed between methods, the more precise methods being, in general, computationally more complex. The aim of this paper is to provide both theorists and experimentalists with benchmarks to decide which method is the most appropriate for a particular application and to gauge the errors associated with each one.

Keywords Contact mechanics, Surface Roughness Analysis and Models

PACS 46.55.+d Tribology and mechanical contacts · 68.35.-p Solid surfaces and solid-solid interfaces: structure and energetics · 68.35.Gy Mechanical properties; surface strains

1 Introduction

2016 marked the 50th anniversary of the pioneering work by Greenwood and Williamson (GW) on the contact mechanics of nominally flat, but microscopically rough surfaces [1]. The goal was to explain the widely believed linear variation of contact area with normal load [2] by defining the problem and providing an analytical solution to it.

The debate is not yet closed. The field of contact mechanics still thrives, in part due to theoretical advances in reducing a highly complex problem to one that can be handled on small-scale computers. The arguably most prominent publications on contact mechanics since the GW paper are the proposition by Whitehouse and Archard [3] to describe the surface topography as random and fractal, the GW-inspired work of Bush, Gibson, and Thomas [4] as well as the scaling theory proposed by Persson [5]. There has also been much progress in brute-force solutions to the contact problem. It is now possible to simulate systems that are sufficiently large to mimic the multi-scale nature of surfaces, while reaching the continuum limit through an adequately fine discretization [6, 7].

Comparisons between theoretical predictions and rigorous simulations — making no uncontrolled approximations beyond the model assumptions — are usually limited to the question of whether a model reproduces the linearity between load and contact area [6, 8–11]. Such comparisons are weak tests, since theories merely need to reproduce a single proportionality coefficient while they usually depend on more than one adjustable

parameter, which may not even be well defined from experiment or the model definition. The adjustable parameter thereby becomes effectively a fitting parameter. An important example of such a term is the scale-dependent radius of curvature of an asperity [12], which plays a critical role in asperity-based models.

Comparisons of theories and rigorous simulations beyond the proportionality coefficient of load and true contact area have been scarce. Notable examples are the analysis of the following quantities: the gap-distribution function [13], the dependence of mean gap or contact stiffness on load [14, 15], or the interfacial stress spectrum [16, 17].

To date, the few in-depth comparisons between theory and rigorous simulations have mainly focused on adhesionless contacts. Rigorous comparison for adhesive interfaces have been even more scarce. The reason for this may be that modeling short-range adhesion in continuum models places large demands on simulations, while longer-range adhesion in multi-asperity contacts is usually arduous to describe theoretically. In fact, handling short-range adhesion in simulations of single-asperity contacts and reproducing (closely) the famous analytical results by Johnson, Kendall, and Roberts (JKR) [18] is not an easy task. A fine discretization is required close to the contact line [19], which is sometimes also called a contact edge. Thus, a rigorous, numerical approach to short-range adhesion in mechanical contacts remains a demanding exercise.

Due to the lack of rigorous tests, it is difficult for theorists to choose the most appropriate contact-mechanics method. For experimentalists it is hard to know whose results and whose interpretations to trust. For this reason, it was decided to pose a contact-mechanics challenge [20] — very much in the spirit of the Sandia fracture challenge [21] — allowing theorists and modelers alike to test the reliability of their preferred method. The challenge was made public in early December 2015 on arXiv.org [20] and further announced to the tribological community in a Cutting Edge article [22]. The final deadline for the submission of results was June 30, 2016. The reference results, which had been produced by the authors of the challenge, remained undisclosed until all results were received.

In the following, we describe the posed challenge in Section 2. The various solution strategies are sketched in Section 3. The results are presented in Section 4 while the final Section 5 compares and contrasts the various approaches and their complexity, and provides an estimate of the precision of each method.

2 Definition of the Challenge

This section contains the original description [20] of the model on which the contact-mechanics challenge was based. We avoid reiterating quantities to be computed, as this will become evident in the results section. However, a note was added on how to rescale parameters (in particular the surface topography and its root-mean-square gradient), so that the mathematical equations to be solved remained unchanged. This was done to address a criticism that the problem definition violates the small-slope approximation or exclusively pertains to soft-matter contacts.

Our surface topography was produced by drawing random numbers for the Fourier transform of the height profiles $\tilde{h}(\mathbf{q})$ having a mean of zero and, on average, a second moment defined by the height spectrum

$$C(q) \equiv \langle |\tilde{h}(\mathbf{q})|^2 \rangle \quad (1)$$

$$= C(q_r) \times \begin{cases} 1 & \text{for } \lambda_r < 2\pi/q \leq \mathcal{L} \\ (q/q_r)^{-2(1+H)} & \text{for } \lambda_s \leq 2\pi/q < \lambda_r \\ 0 & \text{else.} \end{cases}$$

Here, $\mathcal{L} = 0.1$ mm is the linear dimension in x and y of the periodically repeated simulation cell, $\lambda_r = 20$ μm is the roll-off wavelength, $q_r = 2\pi/\lambda_r$, and $\lambda_s = 0.1$ μm is the short-wavelength cutoff, below which no roughness is considered. $H = 0.8$ is the Hurst roughness exponent [23]. A graph showing the spectrum is presented in Fig. 1. The features of the spectrum are similar to those found experimentally for a wide variety of surfaces [24,25].

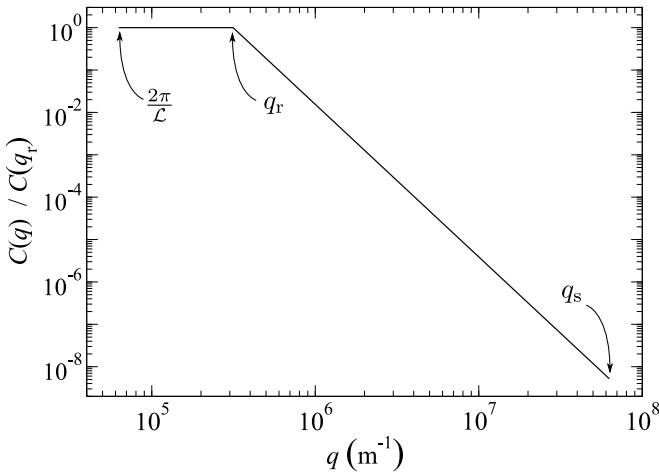


Fig. 1 Height spectrum $C(q)$ from which the height distribution is drawn. It is normalized to its value at the roll-off wavenumber q_r .

It might be argued that introducing a small-wavelength cutoff is artificial. However, it was found to be necessary

in order to be able to compare simulations to continuum theories. For similar reasons, a hard-wall interaction was preferred over finite-range repulsion. Even if the latter might be more realistic and, in some ways, easier to handle numerically (e.g., when relaxing the displacement field with a conjugate-gradient method), a hard-wall repulsion allows the interfacial separation u to be unambiguously determined. Contact can then be defined to occur where $u = 0$.

The resulting surface topography arising from the spectrum is depicted in Fig. 2. The height spectra were normalized such that the root-mean-square gradient of the height is $\bar{g} = 1$. Furthermore, the heights were shifted such that their minimum value is zero. Further characteristics of the surface topography are: mean height $\langle h \rangle = 2.633$ μm , maximum height $h_{\text{max}} = 5.642$ μm , with a root-mean-square height fluctuation of $\sqrt{\langle \delta h^2 \rangle} = 0.762$ μm and where $\langle \delta h^2 \rangle \equiv \langle h^2 \rangle - \langle h \rangle^2$. The inverse root-mean-square curvature, which one may interpret as a typical local radius of curvature, is $R_c = 60$ nm.

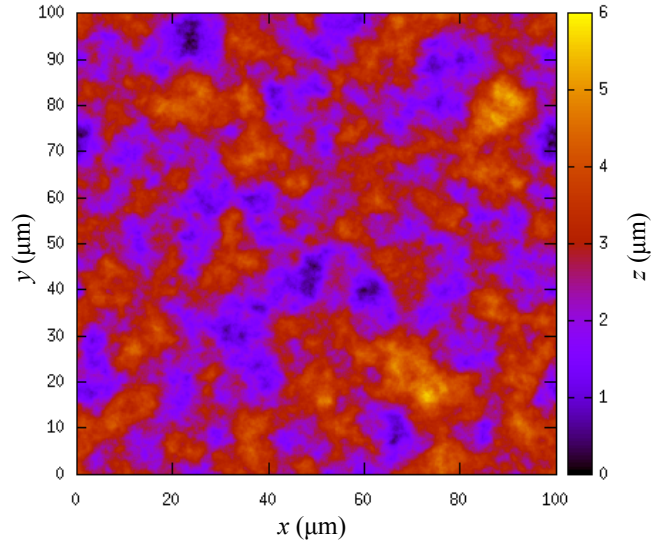


Fig. 2 Height profile of the random surface that was produced from the spectrum shown in Figure 1.

The surface is pressed down against an originally flat, elastic manifold. Thus, the first points of contact occur at small height, i.e., at the dark areas of Fig. 2.

2.1 Elasticity, external load, and adhesion

The small-slope approximation is assumed, which forms the basis for essentially any contact mechanics theory. All roughness is mapped to the indenter, while all compliance is assigned to the substrate with a contact modulus of $E^* = 25$ MPa, which is characteristic of rubber.

Here, $E^* \equiv E/(1-\nu^2)$, where E is the Young's modulus and ν is Poisson's ratio. We leave the individual terms E and ν unspecified, because we focus exclusively on normal displacements.

The external default pressure acts homogeneously across the system. It is set to $0.01 E^* \bar{g} = 250$ kPa. In other words, the total load on the simulated area of 0.01 mm^2 is 0.0025 N . The elastically deformable solid is assumed to be semi-infinite. Like the rigid substrate, it is periodically repeated in the plane.

Short-range repulsion is realized with a hard-wall interaction; the indenter is not allowed to penetrate the rigid substrate. In addition, the two surfaces interact with a finite-range adhesion according to

$$v[g] = -\gamma_0 \int d^2r \exp\{-g(\mathbf{r})/\rho\}, \quad (2)$$

where $\gamma_0 = 50 \text{ mJ/m}^2$ is the surface energy at perfect contact, $g(\mathbf{r})$ is the local gap or interfacial separation (in geology also aperture) as a function of the in-plane coordinate \mathbf{r} , and $\rho = 2.071 \text{ nm}$. We note that the exponential cohesive-zone model used here gives essentially identical results to the analytical solutions of Maugis [26], who used Dugdale's model for adhesion, see Figs. 9 and 10 in Ref. [19].

Defining a local Tabor coefficient according to $\mu_T \equiv R_c^{1/3}(\gamma_0/E^*)^{2/3}/\rho$, we obtain $\mu_T = 3$. This value can certainly be classified as short-range adhesion. See also Figs. 9 and 10 in Ref. [19], where it is also evident that $\mu_T = 3$ is close to the JKR limit of infinitely short-range adhesion, at least as far as contact radius and normal displacement are concerned.

The parameters were chosen to mimic the contact between rubber and a highly polished surface, although the contact modulus may be somewhat at the upper range of practical applications. However, the model was constructed such that there is no significant adhesive hysteresis up to moderate contact pressures, otherwise, functional relations such as $\bar{u}(L)$ or $a_r(L)$ would become history dependent, thereby impeding comparisons between theoretical predictions and our simulations.

Pastewka and Robbins [27] found that surfaces only became hysteretic or "sticky" when the ratio of "repulsive" contact area and load no longer increases linearly with pressure at small contact area. We found similar results [28] and thus chose an adhesion such that the total contact area is increased by roughly 50% compared to the adhesionless case — at relative contact areas of a few percent.

2.2 Summary and discussion of default parameters

Two important dimensionless quantities of our default problem are the Tabor parameter $\mu_T = 3$ and the surface root-mean square gradient $\bar{g} = 1$. Additional quantities in SI units are: $E^* = 25 \text{ MPa}$, $\gamma_0 = 50 \text{ mJ/m}^2$, $\rho = 2.071 \text{ nm}$, system size $\mathcal{L} = 0.1 \text{ mm}$, externally applied pressure $p_0 = 250 \text{ kPa}$.

It might be beneficial to use a problem-adapted unit system, which is what was done by MHM and WBD in the reference simulations. In this unit system one has: $E^* \bar{g}$ as the unit for pressure and \mathcal{L} as the unit for length. One can then use $E^* = 1$, $\mathcal{L} = 1$, $p_0 = 0.01$, $\gamma_0 = 2 \times 10^{-5}$, and $\rho = 2.071 \times 10^{-5}$.

Also note that the (linearized) force balance equations to be solved remain unchanged, for example, by the following substitutions reducing the rms gradient to half of its original value: $\tilde{h}(\mathbf{q}) \rightarrow \tilde{h}(\mathbf{q})/2$, $\rho \rightarrow \rho/2$, $\gamma \rightarrow \gamma/2$, and $E^* \rightarrow E^*/2$. Thus, while it might appear risky to use the small-slope approximation for the default surface having an rms-gradient of one, it is a straightforward procedure to redefine the problem such that \bar{g} is indeed negligible compared to unity, e.g., by repeatedly executing the above-mentioned rescaling.

Owing to the possibility of rescaling the mathematical problem to smaller scales, one can redimensionalize it such that it becomes a contact problem at smaller scales and harder materials.

3 Solution strategies

The different strategies adopted to tackle the contact challenge – all numerical or theoretical except for one experimental – are summarized in this section. They are described in the order of the date of submission. The first described method, using Green's function molecular dynamics, is referred to as the **reference solution**, primarily because it was pursued by the author posing the challenge (MHM), but also because it is based on the finest discretization of all submissions while avoiding any uncontrolled approximations. Since the number of submissions was large, each method is only sketched briefly to keep the paper at a reasonable length. However, all participants of this challenge either cite published work, in which their method is described, or, plan on writing a detailed follow-up paper.

Before presenting the approaches, we wish to clarify that the nomenclature of each method was assigned with some degree of arbitrariness. In most cases, it simply reflects what technical terms contributors emphasized the most in the description of their work. Many methods could be classified as Green's functions or boundary-

value or biconjugate-gradient stabilized methods. However, we tried to avoid multiple uses of similar terms.

3.1 Green’s Function Molecular Dynamics

One numerical strategy is the Green’s function molecular dynamics (GFMD) [29] method, which two of us (MHM and WBD) used here, as described in reference [7]. The short-range adhesion places large demands on the discretization. Reaching convergence necessitates fine discretization, in particular for adhesive necks forming near contact lines. We found that a discretization scale of $a = \lambda_s/64$ was sufficient for most purposes and consequently produced reference data on systems with $64k \times 64k \approx 4 \times 10^9$ discretization points on the surface. In some cases, we used $a = O(\lambda_s/128)$ or $\approx 16 \times 10^9$ grid points to ensure that the results were close to the continuum limit. Setting the damping such that the slowest mode of the system, i.e., the center-of-mass mode, to be slightly underdamped, the system can be typically relaxed within a few thousand time steps, although equilibration at the smallest investigated loads, resulting in 0.3% relative contact area, necessitates roughly ten times more simulation steps.

3.2 FFT based boundary-value method

A fast-Fourier-transform (FFT) based boundary-value method (BVM) was adopted by four co-authors (RB, PS, NL, and AAL) and denoted as FFT-BVM. The usual way of treating a normal contact without adhesion as a classical boundary-value problem would be to minimize the total potential energy with respect to the stress field through a conjugate gradient-iteration scheme obeying two constraints: the stress in the non-contact zone must be zero and there may be no penetration of the two solids [30]. The constraints are realized by removing points with negative pressure from the contact at each iteration step while adding overlapping points to it. The interdependence between stress and strain fields is best computed in Fourier space, while transforming between real and Fourier space representations with an FFT method [31].

In the current approach, the displacements in the non-contact regions were taken as unknown variables rather than the stress in the contact. This procedure proves to be more robust in the presence of adhesion than the traditional scheme, which appears advantageous for non-adhesive contacts. Simulations were run on a single CPU with a 16384×16384 grid for most cases, and on a 32768×32768 grid for the reference point.

3.3 Persson theory

One of the contributors to this paper, BNJP, used his own theory [5] to tackle the problem. Its fundamental concept is to solve the problem first at a coarse scale by neglecting all random roughness and to include the effects that random roughness has on mean values or distribution functions (e.g., for contact stress and mean interfacial separation) by successively including ever finer details of the height profiles into the calculation. The approach, simply named “Persson” hereafter, has been described in various contributions [5,32]. Due to time constraints, adhesion was neglected in this approach for the calculation of distribution functions, although it can, in principle, be included [33,34]. Average quantities such as contact area or mean gap include the effect of adhesion. In a complementary work, more details as well as additional results are presented [35].

3.4 Experiment

Six of the contributors (KH, AB, KS, SR, PI and WGS) set up real-laboratory experiments mimicking the assigned challenge. The pertinent data are denoted as “experiment”.

The surface was scaled globally by a factor of 1000 to produce a model $10\text{ cm} \times 10\text{ cm}$ in plane and approximately 10 mm out-of-plane. The corrugated surface was 3D printed as solid object with an opaque polymethylmethacrylate (PMMA) print material and a resolution of $16\text{ }\mu\text{m}$ in all directions. The countersample was molded with polydimethylsiloxane (PDMS). It was produced with the appropriate base/agent ratio to match the dimensionless surface energies as well as possible. The contact was imaged using a D800 camera with 36.3 megapixels CMOS sensor looking through the bottom of the counter-sample and focused on its free surface. A frustrated total-internal-reflection method was used to image the contact area. A manuscript containing details of the method has already been submitted. (add reference in proof)

3.5 Winkler foundation approach

Two contributors (TA and WGS) tackled the contact mechanics challenge with a Winkler model, which uses independent elastic elements. Elements touching the counter-surface are compressed in order to avoid mutual overlap thereby leading to a force that is linear in the displacement of the elements from the center of mass of the Winkler foundation. The elements surrounding each contact patch are extended to touch the

counter-surface. This was done by dilating each contact patch until it was twice its original area (keeping the inner part compressed and extending the outer elements). The method was chosen because it conserves volume when indenting a sphere into a flat surface. As such the simulations were meant to reflect an elastic system with a Poisson number close to 0.5, roughly reflecting PDMS used in the experiments, see section 3.4.

The spring stiffness was adjusted empirically to match the relative contact area for the reference system. This led to a spring stiffness of $k = E^* \bar{g} \lambda$ with an effective thickness of $\lambda = 1 \mu\text{m}$ for the assigned problem.

3.6 Spatially resolved Greenwood-Williamson

Three contributors (HAE, MK, and SA) submitted the first modification of a Greenwood-Williamson inspired approach. However, rather than first taking statistics of asperity heights and curvatures, summit heights were determined individually and the JKR equations are solved individually for each summit. The method is therefore called spatially resolved Greenwood-Williamson (SRGW). The tips of asperities were identified as those points whose eight neighboring grid points are more distant from the flat counterface than the considered central point. Radii of curvature were determined through spline fitting. The contribution to the total load was added up for each individual asperity.

3.7 Biconjugate-gradient stabilized method

One contributor (JJW) used a “biconjugate-gradient stabilized method” [36], which is denoted as BICGSTAB hereafter. As with many other methods pursued in the contact challenge, BICGSTAB used (inverse) fast Fourier transforms to relate displacements and strains. The repulsion was recast as a high-order power law, to avoid problems due to hard-wall interactions. This was done, because not only first but also second-order derivatives of the energy function should be defined for a conventional biconjugate gradient method to work properly. Also the adhesive part was modeled with a power law rather than with an exponential function. Specifically, the following cohesive zone model was employed

$$\gamma(g) = \frac{8\gamma_0}{3\rho} \left[\left(\frac{\rho}{g} \right)^9 - \left(\frac{\rho}{g} \right)^3 \right], \quad (3)$$

where $\gamma(g)$ describes the surface energy gained per unit area at a given interfacial separation g . Note that the hard-wall limit can be approached in principle, by using

a larger and larger exponent for the repulsion, however, small exponents are beneficial, from a numerical point of view. The surface was discretized into 512×512 , or, in some cases, 1024×1024 grid points.

3.8 Boundary-element method with B-spline interpolation

Two contributors (GV and AV) numerically solved the Boussinesq equation combined with the specified adhesive potential numerically by using an improved version of their in-house implementation of the boundary-element method (BEM) [37–39] to minimize the total energy of the system. Within their numerical scheme, the total (elastic plus adhesive) energy was minimized by varying the displacement field. An augmented Lagrangian formalism was applied to satisfy the hard-wall constraint.

The bandwidth was limited to wavelengths $\lambda > \mathcal{L}/256$. The displacement field was interpolated using periodic cubic B-splines with 1024×1024 degrees of freedom. This allowed the contributors of this method — called BEM+B hereafter — to run all calculations on a standard desktop PC with a typical computation time of two hours per configuration. As in other methods, the problem was solved in Fourier rather than in real space. A detailed description of this method is planned to be published by GV and AV in a forthcoming paper.

3.9 All-atom MD

Two contributors (SS and AIV) tackled the problem using all-atom simulations. This approach is denoted all-atom MD. To render the solution of the problem computationally feasible, the system was scaled to atomic dimensions, such that the atomic bond lengths were slightly greater than the scaled-down cutoff at short wavelengths. At the same time, dimensionless numbers describing the contact-mechanics problem were retained as far as possible.

The most important aspects of the approach can be summarized as follows: The all-atom MD approach consists of a rough, rigid indenter with the scaled profile of the defined surface and an originally flat, deformable body made up of individual atoms. The simulation cell had a length of $\mathcal{L} = 97.8 \text{ nm}$ in x and y directions, corresponding to 175 times the lattice constant of calcium, $a_0 = 5.5884 \text{ \AA}$. Moreover, the z -axis of the deformable body was assigned to the $[100]$ direction, which had a depth of $\mathcal{L}_z = 14 \text{ nm}$. At the end of the solid, an additional fixed rigid flat body provided the needed support for the deformable part. Interactions between atoms in

the deformable body were described by an embedded atom method (EAM) potential [40] with the database provided by Sheng *et al.* [41] leading to an indentation modulus of $E^* = 28.57$ GPa. Moreover, the short-range repulsion was governed via a (12-6) Lennard-Jones (LJ) potential, $V(r) = 4\epsilon\{(\sigma/r)^{12} - (\sigma/r)^6\}$ [42], producing a reasonable lattice constant and bulk modulus for calcium with $\epsilon = 0.2145$ eV and $\sigma = 3.5927$ Å [43]. The Lennard-Jones potential was cut off at its minimum and a constant added to constrain force and energy to go smoothly to zero at the cutoff. Adhesion was modeled with the assigned exponential interaction potential, which was adjusted to maintain the dimensionless surface energy and range of interaction at the described values. Atoms were taken to be in contact with the counter body when their distance was less than $d_c = 4.0354$ Å. More information on the method of defining the contact distance in non-adhesive atomistic contacts is available in a recent paper by SS and AIV [44].

Simulations were performed by the GPU package of LAMMPS [45–47]. Post processing was done using OVITO [48], imageJ [49], and a number of in-house codes.

3.10 Two Archard-based models

Four contributors (RLJ, YX, JS, and AR) used an approach inspired by Archard’s multiscale stacked (MS) asperity concept [50]. The approach is referred to as MS-Archard in the following. In this method, small asperities are placed on top of larger asperities, which are then placed on top of even larger asperities, and so on. The net load carried by the asperities at each hierarchy level – or magnification – does not change with magnification. Details of the method for adhesionless contacts are described in the literature [50]. Adhesion was included in the current treatment by using the average gap between the surfaces, which is estimated with a method proposed for surfaces with sinusoidal waviness [51].

RLJ, YX, JS, and AR also submitted results that were obtained with a modification of the original MS Archard concept [50]. The basic idea is to apply a low-pass filter to the true surface topography, which only keeps the smallest wave numbers. The low-pass surface is then represented by an equivalent set of one-dimensional Fourier coefficients using a spectral method proposed by Rostami and Streater [52]. Finally, the surface is subjected to a discretized simulation. The effect of small-scale roughness is incorporated by a roughness layer (RL), which resides on top of the low-pass surface. The RL is constructed such that the summit area

density and the rms curvature of the entire surface is correctly reproduced.

For the computation of the contact area, the Jackson-Streater multiscale model [50] is applied. The fractional contact area of the roughness layer is multiplied with that of the low-pass surface. For the estimation of the mean gap, it is assumed that only the low-pass surface amplitudes are important. The approach is denoted RL-Archard.

3.11 Fast-Fourier-transform integrated adhesion

The two contributors DD and SM also use a FFT based method [53], in which adhesive and contact pressures are stored and relaxed independently within each full iteration loop. The algorithm uses a common conjugate gradient method to solve for the positive contact pressures, whilst the adhesive pressures are relaxed towards a value that corresponds to the proposed surface separation. The contributors made changes to the original work [53] to accommodate the specified exponential adhesive potential. The periodicity of the surfaces favored a transition from a real-space multi-level integration scheme for the elastic deformation to one that is Fourier based.

One of the objectives of this model is to permit a coarse representation of a surface (for computational speed) whilst still being able to capture the key adhesive effects in a local and deterministic manner. The approach taken in the given implementation was to integrate the adhesive pressures between adjacent nodes rather than relying on surface interactions at individual nodes. This procedure should capture part of the adhesive force that can be missed at a steep surface gradient without a fine mesh. The adhesive potential of this challenge also permitted an accurate surface integral over each internode element rather than previous approximations [53]. Since the treatment of adhesion received particular attention, the method is called FFT-IA, where IA stands for integrated adhesion.

A surface mesh of 16384×16384 nodes was used for the reference case and otherwise a relatively coarse mesh size of 4096×4096 . The latter was chosen to test the ability of the integration method to capture the near-contact adhesion, whilst enabling a fast solution time of approximately than 1 hour on a single CPU at 4096×4096 .

3.12 Slightly corrected Greenwood-Williamson

Due to the lack of a contribution based on the original, statistical approach of Greenwood and Williamson, one

contributor (GC) – who teamed up with another (FB) – was personally invited (after the submission deadline) to apply his GW approach [54] to the specified contact challenge. Their data therefore do not reflect the best attempt of these contributors at the challenge, which they would have based on their own boundary-value method [55–57], but rather an analysis of the specified problem in terms of a slightly corrected Greenwood-Williamson approach (SCGW) [54]. The main modification of SCGW with respect to the original GW paper [1] consists of allowing the curvature of the GW asperity tips to depend on the height of the maxima.

It is important to note that the SCGW approach did not include adhesion due to time constraints. As one can see in the result section, neglecting adhesion predominantly affects contact area and local stress or its distribution function but only slightly influences the mean gap. As such, this contribution serves predominantly as a benchmark calculation of how well the SCGW predicts the interfacial separation.

3.13 Interacting and coalescing Hertzian asperities

One of the contributors (GC) to the SCGW approach was given the opportunity to consider another asperity-based model together with an additional contributor (LA). They used an approach in which contact patches that start to overlap are merged together into a single, larger-scale coalesced asperity [58]. The underlying approach is denoted as the interacting and coalescing Hertzian asperities (ICHA) approach.

3.14 GFMD-II

Another group (JM, LP, and MOR) was invited after the deadline to contribute to the challenge and to clarify some original discrepancies between two solutions that agreed in all but one single quantity. Their approach is also based on GFMD, although the code was developed completely independently of that by MHM and WBD, see section 3.1.

3.15 Brief comparison of pursued approaches

Before analyzing the results in detail, it is worth comparing and categorizing the approaches pursued in this study. One class of strategy, "brute-force computing", makes no *uncontrolled* approximations to the assigned mathematical models, namely, GFMD, FFT-BVM, BIC-GSTAB, BEM+B, and FFT-IA methods. The results of these methods should approach the exact values when

the employed mesh sizes are sufficiently small given that the code effectively minimized the total energy with respect to the displacement or stress fields. Brute-force methods may very well differ in how closely they approach an exact result at a given discretization or how many iterations or floating point operations are needed to identify a solution at a required accuracy. A brute-force method is termed efficient if it closely approaches the exact solution even using a coarse mesh and if it requires only a few iterations to find the solution for a given mesh.

All additional (numerical) methods in this study (Persson, Winkler, SRGW, all-atom MD, MS/RL-Archard, SC-GW, and ICHA) do not solve the assigned partial differential equations subjected to the given boundary conditions. Instead all these methods except the all-atom MD simulations make use of physical or mathematical arguments leading to equations that require either much less computing time and/or less coding time than the brute-force approaches. There is thus a trade-off between accuracy and cost, which is why the methods cannot be unambiguously ranked unless one predicts all observables more accurately than another with a lower computational cost. To facilitate the discussion, we refer to models using local constitutive stress-strain equations as bearing-area models (Winkler, SRGW, MS/RL-Archard, SCGW, ICHA), all of which except Winkler are also referred to as asperity-based models, since Winkler only uses local springs, but no input from Hertz or JKR.

Two contributions to the challenge stand out in that they violate – by design – some, if not all, of the assumptions and approximations postulated as (virtual) reality. These are the real-laboratory experiment on PDMS surfaces and the all-atom simulations. Neither contribution truly uses the small-slope approximation but realizes surfaces with the assigned rms-gradient of one. Other potentially severe "limitations" are the long-time visco-elastic-like responses that can occur in the experiments while the all-atom simulations may (and do) show a substantial amount of plastic deformation in the form of dislocation activity. Including these contributions to the challenge despite their restrictions is nevertheless valuable as their results shed light on the question as to what extent the challenge is merely a mathematical exercise, or if it relates to real (experiments) or realistic (all-atom MD based on realistic interatomic potentials) cases. The appeal of these two contributions is also that the linear system size was in one case scaled up by a factor of 1000 from the assigned 0.1 mm scale to 10 cm (experiment) and, in another, it was scaled down by a factor of 100 to 100 nm (all-atom MD). The apparent contact areas in these two

approaches thus differs by ten orders of magnitude in absolute units.

4 Results

This section compares and contrasts the results of the various approaches. It is divided into three parts: In the first, the predictions of spatially resolved observables are compared, for example, the stress at a given reference load across a selected path. Only the methods keeping the surface topography in the computer memory – along with displacement and stress fields – can provide this information. The second part compares predictions of distribution functions, e.g., probability densities of interfacial separation or interfacial stress, again at the default load. Observables of this type can be predicted, in principle, by any stochastic approach to contact mechanics. In the third part, the focus is on questions of how global averages (such as real contact area or mean gap) depend on load or the range of adhesion. These are the properties that are usually measured experimentally. However, reproducing a few of those numbers, e.g., the proportionality coefficient between real contact area and load at small loads, does not mean that the correct answer was produced for the right reason. It might also have been fortuitous or achieved by varying adjustable parameters. In contrast, the correct reproduction of the complex, multi-scale displacement or stress field cannot happen fortuitously.

4.1 Spatially resolved observables

To set the stage for quantitative comparisons and to demonstrate that the assigned challenge relates to large and small scales alike, we compare the contact topography of our reference solution (GFMD) in Fig. 3 with the two submissions, having taken the liberty of changing the 100 micron scale of the problem to 10 cm (experiment) and to 1 micron (all-atom MD). One can certainly recognize an excellent agreement of the overall features, which can be seen as surprising in light of the following reasons: (a) the experiment and all-atom MD use the assigned root-mean-square gradient of one, while GFMD employs the small-slope approximation by design, (b) there are significant deviations from linear elasticity including strong dislocation activity in the all-atom MD and long-time-relaxation processes of PDMS in the experiments, (c) the surface energies supposedly do not match very well, (d) no periodic boundary conditions are employed experimentally, and (e) all-atom MD includes thermal vibrations but violates the con-

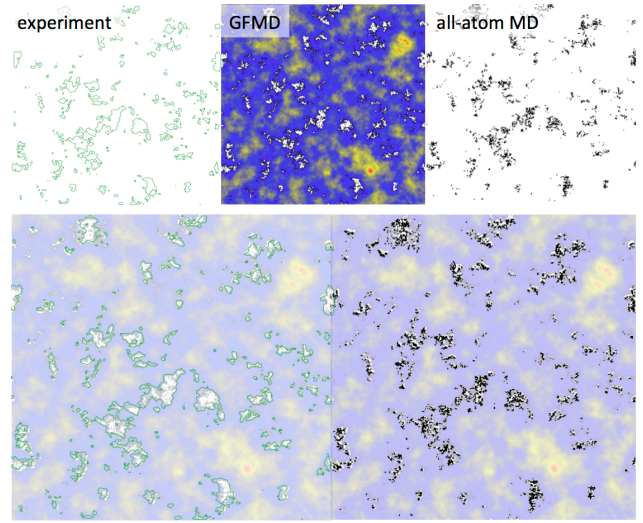


Fig. 3 Comparison of contact geometries. The upper left panel shows the experimentally deduced contact lines, the center top panel the gap topography obtained with GFMD (white is contact, gaps from small in black through blue and yellow to large in red), and the upper right panel shows atoms in contact (black point) as obtained by all-atom MD. The lower row shows the superpositions of GFMD with experiment (left) and with all-atom simulations (right).

tinuum approximation at the smallest scales – both in contradiction to the problem definition.

Usually, one would want to model any of the above-mentioned effects, which were purposefully neglected in the assignment of the challenge to pose a well-defined mathematical problem. Given the close resemblance of the contact topography, one may now argue that only the desire to predict special observables, such as the amount of plastic deformation, would warrant the tremendous effort needed to go beyond the usual assumptions of small slope and linear elasticity.

To ascertain how different methods predict the overall gap topography, we compare the profile of the gap (the interfacial separation between substrate and indenter) along the path $0 \leq y < 100 \mu\text{m}$ at $x = 50 \mu\text{m}$ in Fig. 4. All brute-force methods, shown in the top panel of Fig. 4, predict almost identical results, at this scale of representation. The approximative methods, presented in the bottom panel of Fig. 4, show a much larger spread in the estimates for the gap topography.

The good agreement between the various predictions for the gap by the “exact methods” can be explained as follows: Differences between the methods predominantly pertain to the resolution, i.e., to small-scale features that are too fine to be noticed at the used scale of representation. Only the BICGSTAB method occasionally shows visible deviations from the other exact methods in some parts of the gap profile, e.g.,

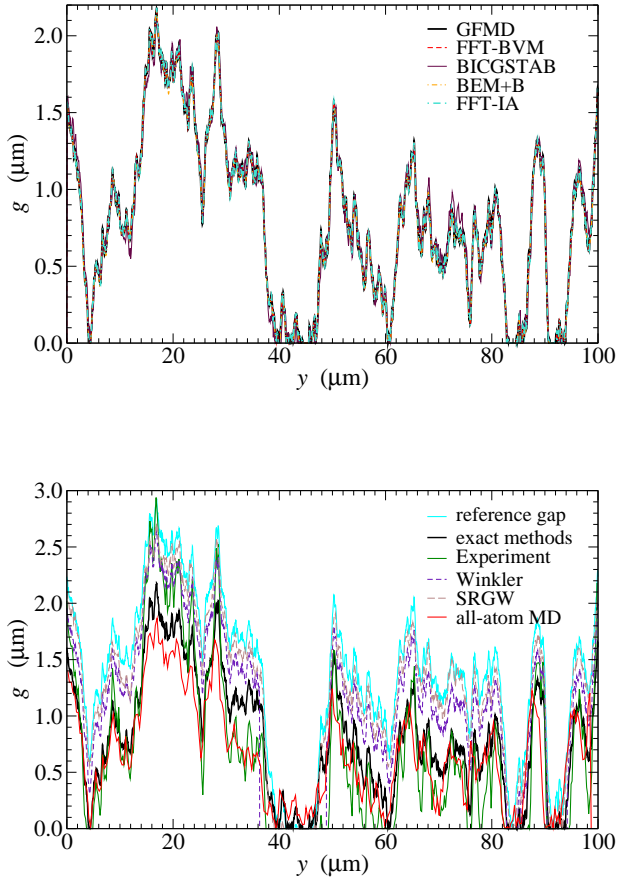


Fig. 4 Gap along the cross section at $x = 50 \mu\text{m}$ as a function of the y coordinate. The top graph shows results from methods containing no uncontrolled approximations, while the bottom graph summarizes remaining data sets. Experimental and all-atom results are transformed back to the scale of the assigned challenge.

near $y = 12 \mu\text{m}$ and $y = 72 \mu\text{m}$. This deviation might have resulted from the redefinition of the infinitesimally short-range repulsion to one that is short-ranged but (controllably) finite.

Conversely, the approximate methods show relatively large scatter in their prediction of the gap cross section. The discrepancy between these data and that of exact methods can also be rationalized. Bearing models, such as SRGW and Winkler foundation, systematically overestimate the gap outside of the contacts, because elastic deformation is neglected in these regions. In particular, outside the contact points, bearing models predict gaps that are essentially parallel to the reference gap, which is the gap of the undeformed surfaces, shifted by a constant distance. It is interesting to note that SRGW and Winkler predict similar gaps outside

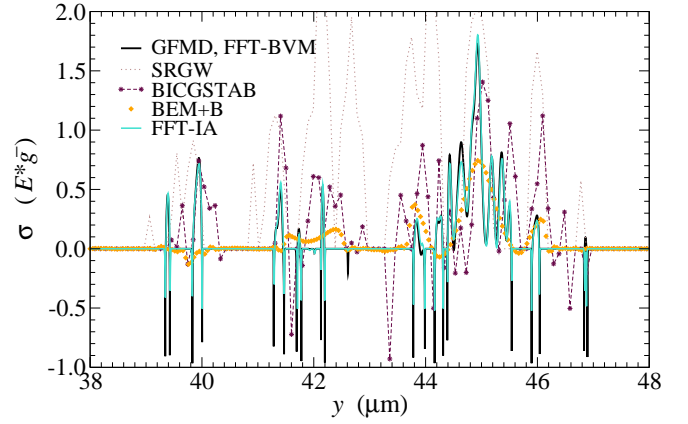


Fig. 5 Interfacial stress along a selected part of the cross section at $x = 50 \mu\text{m}$. GFMD and FFT-BVM agree so closely that no differences can be seen at this resolution.

the contacts, although they are based on rather different micro-mechanical models – unlike SRGW, Winkler would not reproduce the Hertzian contact profile for an ideal parabolic indenter. In contrast, experiment and all-atom simulations either correlate rather well with the reference solution or tend to underestimate the gap. The way in which they do this is highly correlated, despite their quite distinct scales (10 decades discrepancy in the apparent contact area) and distinct physical properties (polymers versus metals). The only obvious common deviation of these approaches from the problem definition is that both experiment and all-atom simulations violated the requested small-slope approximation, because the in-plane coordinates were scaled with the same factor as the normal coordinates in both cases. This kept the rms surface gradient at unity.

Even if the gaps or displacements predicted by the different methods look quite similar at coarse scales, non-negligible differences may occur at small scales. Differences in the solutions become particularly visible in the stress. This is because stress (in the bulk) is a second-order derivative of the displacement field, which in turn makes predictions of the stress much more sensitive to smoothing, finite discretization, or other approximations, than those of displacements. Figure 5 shows how the interfacial stress is expected to vary along a fraction of the cross section at $x = 50 \mu\text{m}$, which was selected to be the largest meso-scale asperity in contact. The interfacial stress is the sum of the adhesive and the constraint force per unit area. In mechanical equilibrium, it is balanced by the internal elastic stress.

GFMD and FFT-BVM agree so closely in their prediction for the stress trace, shown in Fig. 5, such that

differences cannot be spatially resolved. FFT-IA also coincides with the two former methods inside the contact, but it slightly underestimates the adhesive stress close to the contact lines. (At a contact line, i.e., where the gap is positive but still negligible compared to ρ , the range of adhesive interaction, the interfacial stress takes its maximum value of γ_0/ρ , which is approximately one in the chosen unit system. Any deviation from $\sigma = \gamma_0/\rho$ at the contact line does not have to indicate an error in the method or the code but can also arise from integrating the adhesive pressure over the finite area corresponding to a single node, only part of which exhibits the maximum adhesive pressure.)

The BEM+B method can be interpreted as a smeared-out version of the exact solution. BICGSTAB follows the correct trend but shows non-negligible deviations, which are probably due to the redefinition of the hard-wall constraint with short but finite-range repulsion. While SRGW shows the largest discrepancy with respect to the GFMD reference solution, it appears to have the stress peaks at the right positions and, although it generally overestimates the compressive stress, the results reflect the correct order of magnitude.

4.2 Distribution functions

Not every approach to contact mechanics can or should deliver full spatially resolved information on the contact topography or the interfacial stress. In many cases, it is sufficient to know distribution functions, which then allow one to deduce quantities of tribological interest. The three distribution functions considered here are those of contact-patch size, interfacial separation, and interfacial stress. These quantities can be relevant for the following reasons: one may argue that each contact patch contributes to the electrical contact conductivity proportional to the square-root of the contact patch area [59,60]. Thus, knowing the contact-patch-size distribution might enable the electrical contact resistance to be estimated. The gap distribution allows one to estimate quite accurately the resistance to the flow of a liquid through the thin gap between the two solids in contact, in the framework of a (modified) effective-medium theory [61]. Finally, the stress distribution function can shed light on questions such as what fraction of the predicted contact area bears a stress greater than the (macroscopic) hardness of the solids assuming linear elasticity. Its answer would allow one to roughly estimate the relevance of plastic deformation.

In the present context, we are predominantly interested in the various distribution function to ascertain the strengths and weaknesses of different approaches.

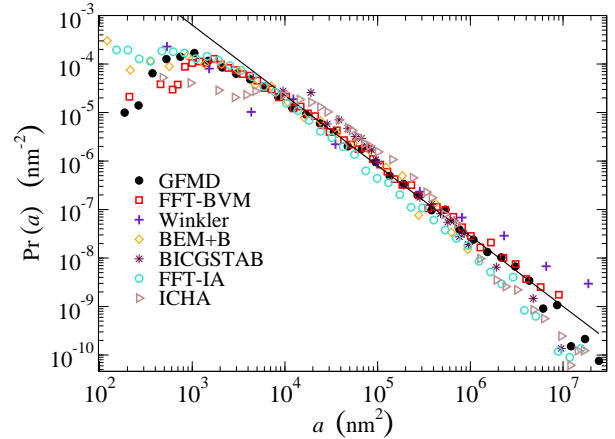


Fig. 6 Contact-patch-size distribution function $\text{Pr}(a)$. The full line indicates the power law $\text{Pr}(a) \propto a^{-1.45}$.

We start our analysis with the contact-patch distribution function, which is not only (implicitly) contained in the “exact”, brute-force approaches but also in bearing-area models such as GW or Winkler.

Greenwood-Williamson-inspired approaches assume a certain distribution of asperity heights and loads that each asperity has to carry. GW-based models therefore implicitly contain statistics about the size of contact patches. To give modelers the opportunity to check these statistics, the probability of a randomly picked cluster to have size a was computed. Results are presented in Fig. 6. GFMD and FFT-BVM find virtually identical results with small differences only at very small and very large cluster sizes. The largest probability density occurs at $a \approx 100 \text{ nm}^2$, i.e., the probability that a randomly picked patch (each patch given the same *a-priori* weight) is largest around that value of a . BEM+B finds excellent agreement with the reference GFMD solution and FFT-BVM. However, the probability of the existence of small contact patches is slightly overestimated. This is probably due to the relatively coarse representation of the surfaces, which is known to lead to an overestimation of the number of small-scale patches from non-adhesive contacts [62]. While the other exact methods and also ICHA (which is still based on a coarse-scale BEM solution) appear to show a similar $\text{Pr}(a)$ powerlaw as those resembling the reference solution, nuances matter, which are discussed further below.

A maximum in $\text{Pr}(a)$, as revealed in Fig. 6 for adhesive contacts by GFMD and FFT-BVM, was not identified in purely repulsive contact in a study by Campa a [62]. Instead, he found an almost constant value of $\text{Pr}(a)$ for

small-scale patches. Apparently, short-range adhesion suppresses the possibility of forming such small-scale contacts, which is in agreement with single-asperity JKR contact mechanics.

To avoid erroneous conclusions from Fig. 6, we also show the cumulative, weighted distribution function in Fig. 7. It is defined as

$$\text{CPr}(a) \equiv \frac{1}{\mathcal{N}} \int_0^a da' \text{Pr}(a') a', \quad (4)$$

where \mathcal{N} is a normalization ensuring that $\text{CPr}(a \rightarrow \infty) = 1$. In the given context, \mathcal{N} simply is the real contact area. The function $\text{CPr}(a)$ describes the fraction of points belonging to a cluster of size less than a , e.g., GFMD and FFT-BVM find that roughly 50% of randomly picked contact points belong to a cluster of a size less than $3 \mu\text{m}^2$, while the remaining points belong to larger clusters. This means that while most clusters are small, most points exist in relatively large clusters: 80% of the contact belongs to patches greater than $1 \mu\text{m}^2$, although the largest number density of clusters is found around $a = 0.001 \mu\text{m}^2$.

Given that $\pi\lambda_s^2$ is approximately only $0.03 \mu\text{m}^2$, one may conclude that most points belong to contact patches whose linear dimensions are much larger than λ_s . The smallest scale, however, predominantly determines local quantities such as rms gradient or curvature. In other words, most contact points belong to meso-scale patches whose linear dimensions are so large that one simply may not treat the asperity with the radius of curvature as measured on top of the asperity at the finest scale.

While the contact-patch distributions of the methods reporting $\text{Pr}(a)$ appeared similar, their cumulative, weighted distributions, $\text{CPr}(a)$ show noticeable differences. The only two methods yielding essentially identical results over several decades are those that found the correct values in the stress at the contact lines, i.e., GFMD and FFT-BVM. Their predictions are also supported by BEM+B, for which statistics were only reported for islands up to $1 \mu\text{m}^2$ size.

Three other methods (BICGSTAB, FFT-IA, and ICHA) fall on another curve in the range $0.1 < a/\mu\text{m}^2 < 1$. The likely reason for the differences in the scaling is that BICGSTAB, FFT-IA, and ICHA defined contact to occur in the points of compressive, interfacial stress, while the other methods defined it as points of zero gap. If we denote a typical contact-patch size a_t to satisfy $\text{CPr}(a_t) = 1/2$, BICGSTAB, FFT-IA, and SCGW find a_t to be a third of the reference solution, which also counted points of tensile stress towards the real contact. In contrast, Winkler and a generic bearing-area model overestimate the typical contact-patch size by a

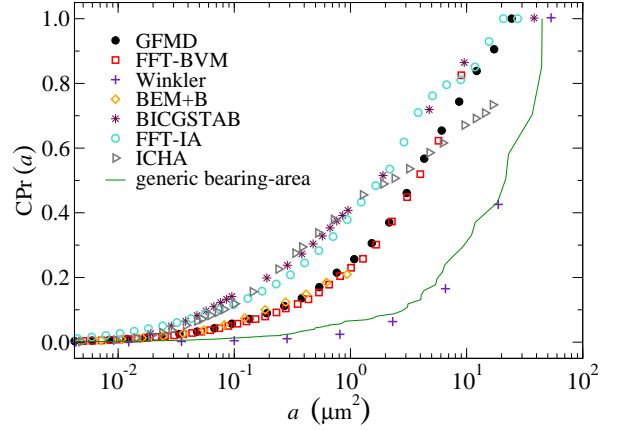


Fig. 7 Cumulative, weighted distribution function $\text{CPr}(a)$, which describes the ratio of contact points belonging to a patch of size less than a . In the generic bearing-area model, the lowest 3% of the surface topography are said to be in contact.

factor of ten. This result is significant given that self-affine roughness extended only over a little more than two decades of wavelength but not unexpected, because bearing-area models predict contact patches to be too localized and therefore too large compared to full solutions that include long-range elasticity [16]. In fact, for the asperity-based model SCGW, which only uses statistical properties of asperity heights, errors turned out to be so large that the results were not included on the graphs.

The gap-distribution function $\text{Pr}(u)$ is discussed next. As mentioned above, it allows one to predict the Reynolds flow through an interface quite accurately. Only solutions that used brute-force methods included adhesion in the calculations of $\text{Pr}(u)$, whereas Persson and ICHA reported results without adhesion. In the latter case $\text{Pr}(u)$ is acquired only for the summit heights. To compare the merits of these two methods and the effect of adhesion on gaps in general, GFMD simulations without adhesion were conducted in order to also provide a reference solution for that case. Results are shown in Fig. 8.

As expected from the spatially resolved gaps in Figure 4, all brute-force methods yield almost identical statistics for gaps exceeding $0.1 \mu\text{m}$. However, distribution functions differ at very small separations. GFMD and FFT-BVM reveal behavior that is typical for short-range adhesion, namely a strongly reduced probability for small gaps due to the formation of adhesive necks near the contact line. (As one moves away from a JKR contact line, the gap quickly increases, while it

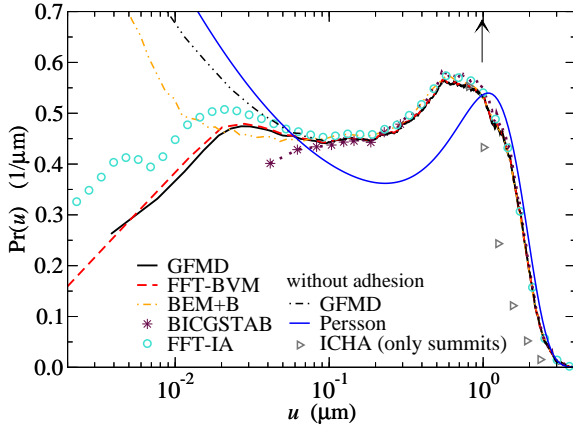


Fig. 8 Gap distribution function for the reference system and for the adhesion-free case. The arrow marks the value of the mean gap yielded by the GFMD reference solution.

increases only slowly – in fact, initially with zero slope – near a Hertzian contact line.) Interestingly, the validity of the BEM+B solution extends all the way down to $2 \times 10^{-2} \mu\text{m}$, even though the bandwidth of the height spectrum was severely limited.

Persson provides good results for the adhesionless case. In particular, the distribution for large gaps is well reproduced, as is the scaling of $\text{Pr}(u)$ for small u . It would be interesting to assess if the theory could also predict the diminution of $\text{Pr}(u)$ for $u \rightarrow 0$, which is induced by short-range adhesion.

The last distribution function to be analyzed is the stress-distribution function $\text{Pr}(\sigma)$. While its shape can be approximated in the absence of adhesion as a sum of two Gaussians that only depend on p^* , $\text{Pr}(\sigma)$ contains much more difficult-to-reproduce features once short-range adhesion is included, see Fig. 9.

The shape of the $\text{Pr}(\sigma)$ can be best rationalized by decomposing it into contact and non-contact contributions. Interfacial stresses averaged only over contact points can be described by a slightly skewed Gaussian, which extends significantly to tensile (negative) stresses. The non-contact stresses lead to a pronounced integrable peak at small negative pressures. This contribution is directly related to the gap-distribution function. The pronounced peak at $\sigma \rightarrow 0^-$ simply reflects that most non-contact points have an interfacial separation that greatly exceeds the range of the adhesive interaction.

As in all other cases, FFT-BVM reproduces the reference solution quite accurately. There is a first instance of an $O(10\%)$ deviation, which can be rationalized by the fact that FFT-BVM uses linear system sizes

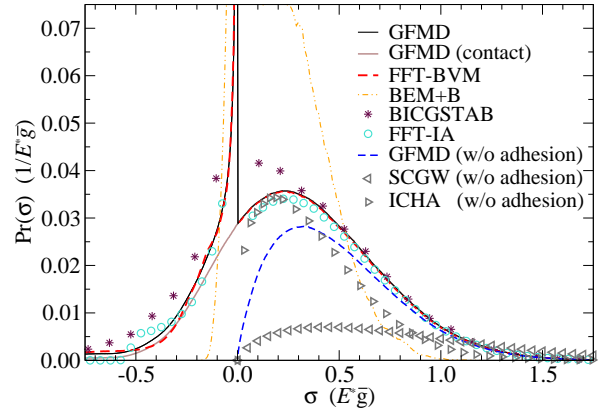


Fig. 9 Interfacial stress distribution function $\text{Pr}(\sigma)$. The peak at slightly negative stresses is due to all points having large local separation, i.e., large compared to the screening length ρ . It contains roughly 97% of the integral below $\text{Pr}(\sigma)$. The contribution to $\text{Pr}(\sigma)$ originating from the true contact area is shown separately for the GFMD method.

of “only” 32,000 instead of 128,000 in GFMD. Despite their much less fine discretization, FFT-IA and BICGSTAB also produce quite accurate stress distributions, in particular for the points in contact. An interesting observation can be made on BEM+B: Due to its limited bandwidth, the stress distribution is not yet quite as broad as it would be if all features were spatially resolved down to the finest scale.

The only two bearing models providing stress distributions, SCGW and ICHA, address the adhesionless case. They must therefore be compared to the GFMD reference data without adhesion. In contrast to SCGW, ICHA model predicts the large-stress tail of the reference solution quite well, although it clearly overestimates $\text{Pr}(\sigma)$ at small σ . A fortuitous side-effect of this error is that the area below the ICHA- $\text{Pr}(\sigma)$ curve, which is equal to the predicted relative contact area, correlates nicely with the contact area of the GFMD reference solution (the area below the grey line in Fig. 9), although the latter includes adhesion. In addition, Fig. 9 reveals that the stress distributions of the adhesive and the non-adhesive cases are quite similar at large stresses. Differences at small stresses must therefore stem predominantly from the zones near contact lines.

4.3 Average quantities

A frequently reported dependence is the relation between relative contact area a_r and load or reduced pressure $p^* \equiv p/E^*\bar{g}$. Many tribologists consider a_r to be

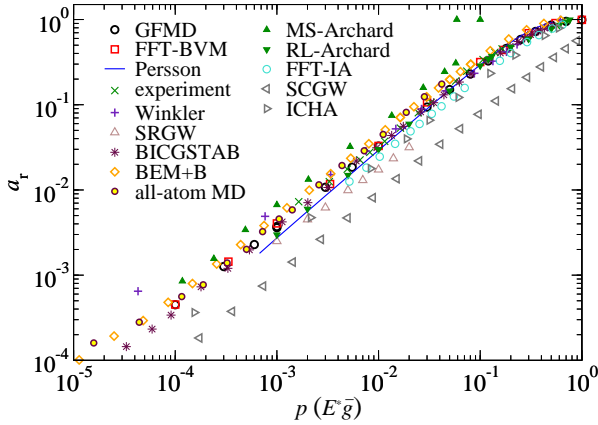


Fig. 10 Relative contact area a_r as a function of pressure p .

one of the most central properties of their field, while others argue that true contact area is hard to define rigorously outside of continuum mechanics, so that reporting it is a purely academic exercise. In continuum mechanics, true contact can correspond to either zones of compressive, interfacial stress or areas that lie within the lines formed by local stress maxima [?]. Since the challenge is formulated as a continuum mechanics problem and contact mechanics has traditionally focused on predicting a_r as a function of load, a discussion of the $a_r(p^*)$ dependence should be included here. For non-adhering, randomly rough surfaces $a_r(p^*) \approx 2p^*$ is an excellent approximation as long as a_r is less than 20% [6–9, 56]. An appropriate generalization of the linear $a_r(p^*)$ relationship to large loads is $a_r \approx \text{erf}(\sqrt{\pi}p^*)$ [5], which even describes quite accurately how complete contact at large p is reached asymptotically [7, 63].

Figure 10 compares the various predictions of $a_c(p^*)$ with weak adhesion. For the most part, they reveal rather similar behavior in a double-logarithmic representation. The difference between most methods and the GFMD reference solution is within the symbol size, i.e., within $\pm 20\%$.

Some – not all – bearing-area models show significant discrepancies with the reference solutions for parts of the $a_c(p^*)$ relationship. The SCGW model, which is based on the statistical analysis of asperity heights, underestimates the quasi-proportionality between a_c and p^* by almost a factor of two. When the actual asperity distributions are considered, as in SRGW and ICHA, much better agreement is found. In the latter model, a_c falls slightly below the reference data, which is not surprising as ICHA was exempted from having to include adhesion. Winkler predicts improper scaling of

a_c with p^* at small p^* , i.e., the dependence is much more sublinear than that of the reference solution.

MS-Archard slightly overestimates a_r , although the behavior only becomes qualitatively incorrect at a jump-into-contact instability, occurring slightly above 30% contact. This is, of course, a range that has certainly not been targeted by asperity-based models. Like MS-Archard, other asperity-based models, such as Winkler, find full contact at relatively moderate pressures. In contrast, Persson’s data are consistent with a smoother disappearance of non-contact area. This issue becomes clear when analyzing the mean gap \bar{u} as a function of p^* .

Differences between the various contact-area predictions are better resolved in Fig. 11, in which the mean contact pressure $\bar{p}_c \equiv p/a_r$ is shown as a function of the external pressure rather than the relative contact area a_r . Small discrepancies now even appear between the otherwise almost identical results of the reference solution and FFT-BVM. They could arise to some degree from multi-stability related to (hysteretic) contact formation or destruction of individual contact patches, saddle points, or dimples. In fact, a given method can produce slightly different results for \bar{p}_c at a given value of p during compression and decompression. However, the trends of all brute-force approaches and to some degree also RL-Archard (which, however, contains a boundary-value method at coarse scales) is such that p_c changes by less than 50% while the external load increases by three decades. It is tempting to speculate that this range would become larger if the ratio of roll-off and short-wavelength cutoff were increased. Persson theory somewhat overestimates the mean pressure at very small values of p . However, as reported in an accompanying paper [35], the slight negative slope of Persson’s prediction of $a(p^*)$ at small p^* is not inherent to the theory but the consequence of an insufficiently fine discretization of the stress histogram. As before, the difference between FFT-IA and the other exact methods is probably due to FFT-IA only having counted points of compressive, interfacial stress towards the real contact area. Lastly, ICHA, which neglected adhesion, identified the correct asymptotic value of the mean contact pressure at small loads, i.e., $p_c \lesssim p/2E^*\bar{g}$ [6, 8, 9, 7] for adhesionless contacts.

Another interesting contact property is the mean interfacial separation, or the mean gap, \bar{u} , between the two surfaces. The reciprocal of its change with pressure, i.e., $dp/d\bar{u}$, also called the interfacial stiffness, is often assumed to be proportional to the electrical contact conductance, so that knowledge of $\bar{u}(p^*)$ allows one to estimate that property [59, 60].

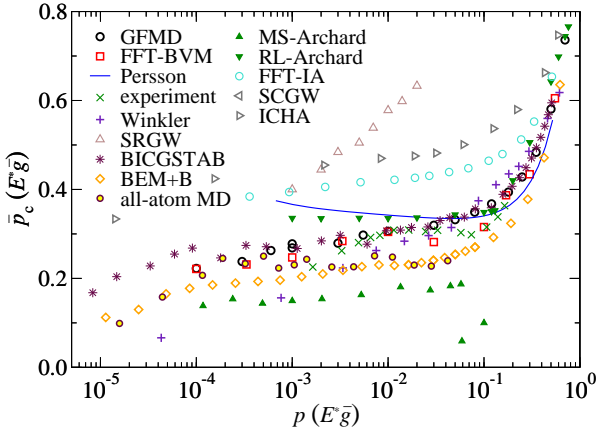


Fig. 11 Mean contact pressure \bar{p}_c as a function of pressure p . The two GFMD symbols at $p = 0.001E^*\bar{g}$ represent a compression (lower circle) and a decompression run (upper circle) coming from zero and large external pressure, respectively. The SCGW data are not shown in this graph as all points satisfy $\bar{p}_c > 0.8 E^*\bar{g}$.

Figure 12 summarizes the predictions of the pressure dependence of the mean gap. As expected from the fully resolved spatial representation of the gap in Figure 4, all brute-force methods agree quite nicely for the mean gap. In a large fraction of the shown pressure range, \bar{u} roughly changes logarithmically with pressure. Persson theory also conveys the correct trend, in particular at $p^* > 5 \times 10^{-3}$. (Details are shown in an accompanying paper [35]. The starting discrepancies at $p^* < 5 \times 10^{-3}$ might be attributed to finite-size effects.)

Bearing-area models do not convey the trend very accurately, although three independent approaches (Winkler, SRGW, and SCGW) make almost identical predictions. For most of the shown pressure range, \bar{u} is overestimated by these bearing models, but then a mean zero gap is approached linearly according to $\bar{u} \propto (p^* - p_{fc}^*)$, for p^* exceeding the pressure $p_{fc}^* \approx 0.8$, where full contact is reached. Both Archard solutions show complete gap closure at an even lower pressure than the other asperity-based models. At small pressures, the RL-Archard method, which solves the low-pass surface topography with a spectral approach, is quite accurate.

ICHA is the only bearing-area model that appears to make the correct predictions at large pressures, however the averages are only taken over peak heights – a full average would have yielded greater mean gaps. In fact, any asperity-based model that provides good – or too small – estimates for the contact area should overestimate the mean gap, because the elastic defor-

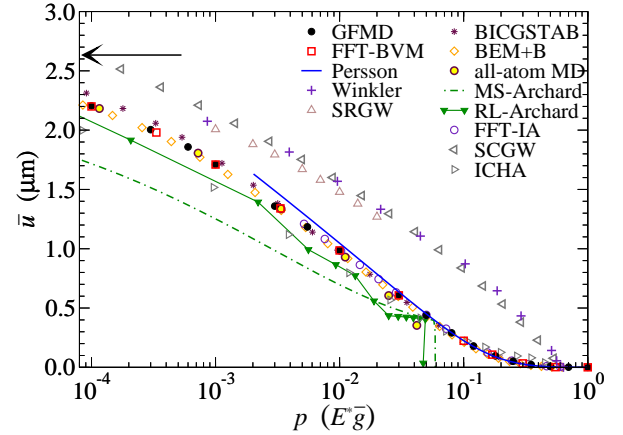


Fig. 12 Mean gap as a function of pressure. The arrow marks the mean gap for the case where a rigid indenter touches the undeformed elastic manifold in a single point.

mation in the non-contact area is neglected. In the specific case of the ICHA model, it is possible, in principle, to include the effect of long-range elastic deformation by considering only the second term of equation (5) in reference [58]. An additional analysis that the contributors of the ICHA model offered to conduct along these lines could not be accepted for time reasons. However, it appears plausible that averaging the gap over all non-contact points while including the effect of elastic deformation outside the contact patches would yield good estimates of the gap for the right reason and not because of fortuitous error cancellation.

In contrast to the bearing models, the brute-force solutions and Persson theory show a more continuous closing of the gap, which, in the range $10^{-4} \leq \bar{u}/\mu\text{m} < 10^{-1}$, can be described by a $\bar{u} \approx 0.3 \cdot \exp(-8p^*) \mu\text{m}$ dependence. Also the all-atom simulations predict the gap to close with pressure in a similar fashion as the continuum-mechanics based calculations. Visible deviations occur at reduced pressures of $p^* \approx 0.04$ yielding relative contact areas slightly exceeding 10%. These deviations correlate with the onset of massive plastic deformation in the simulated metals.

5 Conclusions

The contact challenge attracted participation by many groups world-wide (Austria, England, France, Germany, Italy, Iran, The Netherlands, Taiwan, USA) with 12 competing groups pursuing a total of 13 different approaches. These included traditional Greenwood-Williamson inspired asperity models, the more recent Persson

theory, brute-force computations and even experiments or down-scaling of the problem to all-atom simulations. Each approach was able to reproduce at least some of the reference solutions, which exist because the contact challenge was in fact nothing but a well-defined mathematical problem in continuum mechanics. In this sense, all groups were successful, though some deserve particular mentioning.

The Lubrecht group at INSA Lyon managed to identify the essentially exact reference solution using a Fourier-based approach on a single core with a memory of 150 Gigabyte of random access memory (RAM). This result is also remarkable in that the number of simulated points into which the surface was discretized, 32,000 by 32,000, distinctly exceeds that of most experimental surface topography measurements, which are typically 1,000 by 1,000 and rarely – if ever – more than 4,000 by 4,000. The reported three weeks and 3,000 iterations needed by the Lubrecht group to relax the $32k \times 32k$ surface reduces to one hour and 700 iterations for a $4k \times 4k$ system on a standard laptop with standard RAM and to one minute and 200 iterations for a $1k \times 1k$ discretization on a laptop. This means that highly accurate contact mechanics calculations using experimentally provided height profiles can, in principle, be done in reasonable times with computers available to everybody without having to add extra RAM.

Another remarkable contribution is the experimental work by the Sawyer group at University Florida. The problem was scaled up by a factor of 1,000 and then reproduced thanks to 3D printing technology as a real-laboratory experiment. The optically deduced contact topography at the reference load correlates remarkably well with that obtained by accurate simulations. The experimental contribution thus reveals quite clearly that the challenge has an analogue in the laboratory, and that modelers might have to apologize considerably less for commonly made approximations (e.g., small slopes, linear elasticity) than they frequently do.

Last but not least, the all-atom simulations by the Vakis group in Groningen deserve particular mentioning. They revealed that the posed challenge also relates to metallic systems, albeit at smaller scales. It turned out again that adding features to the problem, which were purposefully neglected in the formulation of the challenge but ubiquitous in most systems (plastic deformation), did not induce large changes in the overall displacement fields or pressure distributions, at least not for the relatively moderate loads used in this challenge.

Overall, there was excellent overall between all rigorous methods, which all described stress-strain relations in Fourier space. Those implementations that min-

imized the total energy with respect to displacement rather than to stresses appeared to have higher resolution. At this point, it is hard to judge if this is generally true, or, if the time commitment by the contributors or the technical details of the respective implementations are responsible for why one code found an almost fully converged answer on single nodes, while others “only” were able to predict the elastic displacement fields correctly at a slightly coarsened scale.

Bearing-area models reproduced the dependence of the contact area on load reasonably well even for relative contact areas clearly exceeding 50%. This is somewhat surprising, since bearing-area models assume positive surface curvature everywhere, while close to full contact, the measure of positive and negative curvature becomes almost identical. In addition, predictions on the interfacial separation – whether the first moment or its distribution – were generally not reliable. This is because bearing-models neglect elastic deformation between the contacting peaks, whereby the gap is overestimated. Surprisingly, the quite simple Winkler model gave almost identical results to the much more sophisticated asperity-based models, except at very small loads, where the Winkler model overestimated the relative contact area. Yet, for both Winkler and bearing-area models, predictions of the mean gap or gap-distribution functions are expected to become even less reliable when the roughness extends to more than 2.5 decades [64]. Also the contact-patch size distribution was rather flawed in asperity-based approaches neglecting the effect of long-range elastic deformation. Since there now exist simple analytical formulae relating contact area and load, one may wonder what the added benefit of conducting such simulations may be, more so as coding a bearing model – with the exception of Winkler – is not necessarily simpler than putting in place a rigorous boundary-value method.

In contrast to other methods with uncontrolled approximations, Persson theory reproduced both the dependence of mean gap and contact area on pressure. Like bearing-area models, Persson theory does not necessitate much computing time, however it is also rather complicated to code. Unfortunately, no predictions were made for the gap or stress distribution in the presence of adhesion, so that we cannot judge (based on the data submitted to the contact-mechanics challenge) how well Persson theory performs for the considered short-range adhesion or whether it would have predicted that $\text{Pr}(u)$ becomes small at small u for short-range adhesion, rather than large, as is the case for no or long-range adhesion.

It might be appropriate to comment on two methods that did not enter the challenge. First, one may notice that no participant used a finite-element method

(FE), although FE should, in principle, be in a position to deliver exact results. It appears, however, that FE is not sufficiently efficient to tackle the assigned problem within reasonable simulation times. Its strength instead lies in its flexibility with respect to geometry and the possibility to go beyond linear elasticity. Second, no work based on Sneddon's method [65] was entered for the competition. It allegedly allows one to distinctly reduce the complexity of a contact problem such that it can be solved in a few minutes on a standard desktop PC. One of the reasons for its absence from this competition may have been that the common formulation of Sneddon's method is only valid for non-adhesive, singly connected domains of spherical symmetry and it rapidly fails once one or two of these assumptions no longer hold. The fact that the considered contact is adhesive, non-spherical, and non-connected, may have kept proponents of the method from comparing their solution to one that they did not know ahead of time [66].

In conclusion, a rather complex contact mechanics problem was successfully solved with a variety of methods. Rigorous, numerical approaches to the posed challenge, which was nothing but a well-defined mathematical problem, found almost identical results on all properties. Small deviations only occurred for those quantities whose computation necessitate a fine grid or arose from different definitions of true contact. Persson theory, experiments, and all-atom simulations all contained uncontrolled approximations to the challenge, but identified the correct trends – and in some cases almost exact numbers for properties beyond the $a(p)$ relationship. Bearing models also predicted the dependence of relative contact area on pressure rather well and additionally offered an alternative interpretation for other properties. Overall, we feel that this challenge has not only assessed the merit of various contact-mechanics approaches but enhanced our understanding of contact mechanics. As such, it could provide a model for future challenges to the tribology community.

Acknowledgements MHM thanks Wilfred Tysoe and Nicholas Spencer for indispensable support in the execution and the write-up of the contact-mechanics challenge. MHM and WBD thank the Jülich Supercomputing Centre for computing time on JUQUEEN. The contribution of GV and AV was funded by the Austrian COMET-Program (Project XTribology, no. 849109) and the work was carried out at the “Excellence Centre of Tribology” (AC2T research GmbH).

Bibliography style needs to be implemented by Tribol. Lett. type setters.

References

1. J. A. Greenwood and J. B. P. Williamson. Contact of nominally flat surfaces. *Proceedings of the Royal Society A: Mathematical, Physical and Engineering Sciences*, 295(1442):300–319, dec 1966.
2. J. F. Archard. Elastic deformation and the laws of friction. *Proceedings of the Royal Society A: Mathematical, Physical and Engineering Sciences*, 243(1233):190–205, dec 1957.
3. D. J. Whitehouse and J. F. Archard. The properties of random surfaces of significance in their contact. *Proceedings of the Royal Society A: Mathematical, Physical and Engineering Sciences*, 316(1524):97–121, mar 1970.
4. A.W. Bush, R.D. Gibson, and T.R. Thomas. The elastic contact of a rough surface. *Wear*, 35(1):87–111, nov 1975.
5. B. N. J. Persson. Theory of rubber friction and contact mechanics. *The Journal of Chemical Physics*, 115(8):3840, 2001.
6. S. Hyun, L. Pei, J.-F. Molinari, and M. O. Robbins. Finite-element analysis of contact between elastic self-affine surfaces. *Physical Review E*, 70(2):026117, aug 2004.
7. Nikolay Prodanov, Wolf B. Dapp, and Martin H. Müser. On the contact area and mean gap of rough, elastic contacts: Dimensional analysis, numerical corrections, and reference data. *Tribology Letters*, 53(2):433–448, dec 2013.
8. C. Campañá and M. H. Müser. Contact mechanics of real vs. randomly rough surfaces: A Green's function molecular dynamics study. *Europhysics Letters (EPL)*, 77(3):38005, jan 2007.
9. G. Carbone and F. Bottiglione. Asperity contact theories: Do they predict linearity between contact area and load? *Journal of the Mechanics and Physics of Solids*, 56(8):2555–2572, aug 2008.
10. M. Ciavarella, G. Demelio, J. R. Barber, and Y. H. Jang. Linear elastic contact of the Weierstrass profile. *Proceedings of the Royal Society A: Mathematical, Physical and Engineering Sciences*, 456(1994):387–405, feb 2000.
11. Marco Paggi and Michele Ciavarella. The coefficient of proportionality κ between real contact area and load, with new asperity models. *Wear*, 268(7-8):1020–1029, mar 2010.
12. J.A. Greenwood and J.J. Wu. Surface Roughness: An apology. *Meccanica*, 36(6):617–630, 2001.
13. A. Almqvist, C. Campañá, N. Prodanov, and B.N.J. Persson. Interfacial separation between elastic solids with randomly rough surfaces: Comparison between theory and numerical techniques. *Journal of the Mechanics and Physics of Solids*, 59(11):2355–2369, nov 2011.
14. Lars Pastewka, Nikolay Prodanov, Boris Lorenz, Martin H. Müser, Mark O. Robbins, and Bo N. J. Persson. Finite-size scaling in the interfacial stiffness of rough elastic contacts. *Physical Review E*, 87(6):062809, jun 2013.
15. Roman Pohrt, Valentin L. Popov, and Alexander E. Filippov. Normal contact stiffness of elastic solids with fractal rough surfaces for one- and three-dimensional systems. *Physical Review E*, 86(2):026710, aug 2012.
16. Carlos Campañá, Martin H. Müser, and Mark O. Robbins. Elastic contact between self-affine surfaces: comparison of numerical stress and contact correlation functions with analytic predictions. *Journal of Physics: Condensed Matter*, 20(35):354013, aug 2008.
17. B N J Persson. On the elastic energy and stress correlation in the contact between elastic solids with randomly rough surfaces. *Journal of Physics: Condensed Matter*, 20(31):312001, jun 2008.

18. K. L. Johnson, K. Kendall, and A. D. Roberts. Surface energy and the contact of elastic solids. *Proceedings of the Royal Society A: Mathematical, Physical and Engineering Sciences*, 324(1558):301–313, sep 1971.
19. Martin H Müser. Single-asperity contact mechanics with positive and negative work of adhesion: Influence of finite-range interactions and a continuum description for the squeeze-out of wetting fluids. *Beilstein J. Nanotechnol.*, 5:419–437, apr 2014.
20. M. H. Müser and W. B. Dapp. The contact mechanics challenge: Problem definition. *ArXiv e-prints*, December 2015.
21. B. L. Boyce, S. L. B. Kramer, H. E. Fang, T. E. Cordova, M. K. Neilsen, K. Dion, A. K. Kaczmarowski, E. Karasz, L. Xue, A. J. Gross, A. Ghahremaninezhad, K. Ravi-Chandar, S.-P. Lin, S.-W. Chi, J. S. Chen, E. Yreux, M. Rüter, D. Qian, Z. Zhou, S. Bhamare, D. T. O'Connor, S. Tang, K. I. Elkhodary, J. Zhao, J. D. Hochhalter, A. R. Cerrone, A. R. Ingraffea, P. A. Wawrzyniek, B. J. Carter, J. M. Emery, M. G. Veilleux, P. Yang, Y. Gan, X. Zhang, Z. Chen, E. Madenci, B. Kilic, T. Zhang, E. Fang, P. Liu, J. Lua, K. Nahshon, M. Miraglia, J. Cruce, R. DeFrese, E. T. Moyer, S. Brinckmann, L. Quinkert, K. Pack, M. Luo, and T. Wierzbicki. The sandia fracture challenge: blind round robin predictions of ductile tearing. *Int J Fract*, 186(1-2):5–68, jan 2014.
22. Wilfred T. Tysoe and Nicholas D. Spencer. Contact-mechanics challenge. *Tribology & Lubrication Technology*, 71:96, 2015.
23. H. E. Hurst. Long-term storage capacity of reservoirs. *T. Am. Soc. Civ. Eng.*, 116:770–799, 1951.
24. A. Majumdar and C.L. Tien. Fractal characterization and simulation of rough surfaces. *Wear*, 136(2):313–327, mar 1990.
25. B. N. J. Persson. On the fractal dimension of rough surfaces. *Tribology Letters*, 54(1):99–106, mar 2014.
26. Daniel Maugis. Adhesion of spheres: The JKR-DMT transition using a dugdale model. *Journal of Colloid and Interface Science*, 150(1):243–269, apr 1992.
27. Lars Pastewka and Mark O. Robbins. Contact between rough surfaces and a criterion for macroscopic adhesion. *Proceedings of the National Academy of Sciences*, 111(9):3298–3303, feb 2014.
28. Martin H. Müser. A dimensionless measure for adhesion and effects of the range of adhesion in contacts of nominally flat surfaces. *Tribology International*, 100:41–47, aug 2016.
29. Carlos Campañá and Martin H. Müser. Practical Green's function approach to the simulation of elastic semi-infinite solids. *Phys. Rev. B*, 74(7):075420, aug 2006.
30. I. A. Polonsky and L. M. Keer. Fast methods for solving rough contact problems: A comparative study. *Journal of Tribology*, 122(1):36, 2000.
31. H. M. Stanley and T. Kato. An FFT-based method for rough surface contact. *Journal of Tribology*, 119(3):481, 1997.
32. B N J Persson, O Albohr, U Tartaglino, A I Volokitin, and E Tosatti. On the nature of surface roughness with application to contact mechanics, sealing, rubber friction and adhesion. *Journal of Physics: Condensed Matter*, 17(1):R1–R62, dec 2004.
33. C. Yang, B. N. J. Persson, J. Israelachvili, and K. Rosenberg. Contact mechanics with adhesion: Interfacial separation and contact area. *EPL (Europhysics Letters)*, 84(4):46004, nov 2008.
34. B. N. J. Persson and M. Scaraggi. Theory of adhesion: Role of surface roughness. *The Journal of Chemical Physics*, 141(12):124701, sep 2014.
35. A. Wang and M. H. Müser. To be filled in by editor.
36. Jiunn-Jong Wu. Numerical analyses on elliptical adhesive contact. *Journal of Physics D: Applied Physics*, 39(9):1899–1907, apr 2006.
37. S. Ilincic, G. Vorlaufer, P. A. Fotiu, A. Vernes, and F. Franek. Combined finite element–boundary element method modelling of elastic multi-asperity contacts. *Proceedings of the Institution of Mechanical Engineers, Part J: Journal of Engineering Tribology*, 223(5):767–776, mar 2009.
38. S. Ilincic, N. Tungkunagorn, A. Vernes, G. Vorlaufer, P. A. Fotiu, and F. Franek. Finite and boundary element method contact mechanics on rough, artificial hip joints. *Proceedings of the Institution of Mechanical Engineers, Part J: Journal of Engineering Tribology*, 225(11):1081–1091, sep 2011.
39. S. Ilincic, A. Vernes, G. Vorlaufer, H. Hunger, N. Dorr, and F. Franek. Numerical estimation of wear in reciprocating tribological experiments. *Proceedings of the Institution of Mechanical Engineers, Part J: Journal of Engineering Tribology*, 227(5):510–519, mar 2013.
40. Murray S. Daw and M. I. Baskes. Embedded-atom method: Derivation and application to impurities, surfaces, and other defects in metals. *Phys. Rev. B*, 29(12):6443–6453, jun 1984.
41. H. W. Sheng, M. J. Kramer, A. Cadien, T. Fujita, and M. W. Chen. Highly optimized embedded-atom-method potentials for fourteen fcc metals. *Phys. Rev. B*, 83(13):134118, apr 2011.
42. J. E. Jones. On the determination of molecular fields. II. From the equation of state of a gas. *Proceedings of the Royal Society A: Mathematical, Physical and Engineering Sciences*, 106(738):463–477, oct 1924.
43. Shu Zhen and G. J. Davies. Calculation of the lennard-jonesn-m potential energy parameters for metals. *Physica Status Solidi (a)*, 78(2):595–605, aug 1983.
44. Soheil Solhjoo and Antonis I. Vakis. Continuum mechanics at the atomic scale: Insights into non-adhesive contacts using molecular dynamics simulations. *Journal of Applied Physics*, 120(21):215102, dec 2016.
45. Steve Plimpton. Fast parallel algorithms for short-range molecular dynamics. *Journal of Computational Physics*, 117(1):1–19, mar 1995.
46. W. Michael Brown, Peng Wang, Steven J. Plimpton, and Arnold N. Tharrington. Implementing molecular dynamics on hybrid high performance computers – short range forces. *Computer Physics Communications*, 182(4):898–911, apr 2011.
47. W. Michael Brown, Axel Kohlmeyer, Steven J. Plimpton, and Arnold N. Tharrington. Implementing molecular dynamics on hybrid high performance computers – particle-particle particle-mesh. *Computer Physics Communications*, 183(3):449–459, mar 2012.
48. Alexander Stukowski. Visualization and analysis of atomistic simulation data with OVITO—the open visualization tool. *Modelling and Simulation in Materials Science and Engineering*, 18(1):015012, dec 2009.
49. W. S. Rasband. imageJ. <https://imagej.nih.gov/ij/>.
50. Robert L. Jackson and Jeffrey L. Streater. A multi-scale model for contact between rough surfaces. *Wear*, 261(11-12):1337–1347, dec 2006.
51. A. Rostami and R. L. Jackson. Predictions of the average surface separation and stiffness between contacting elastic and elastic-plastic sinusoidal surfaces. *Proceedings*

- of the Institution of Mechanical Engineers, Part J: Journal of Engineering Tribology, 227(12):1376–1385, aug 2013.
52. Amir Rostami and Jeffrey L. Streater. Study of liquid-mediated adhesion between 3d rough surfaces: A spectral approach. *Tribology International*, 84:36–47, apr 2015.
 53. Simon Medina and Daniele Dini. A numerical model for the deterministic analysis of adhesive rough contacts down to the nano-scale. *International Journal of Solids and Structures*, 51(14):2620–2632, jul 2014.
 54. Giuseppe Carbone. A slightly corrected Greenwood and Williamson model predicts asymptotic linearity between contact area and load. *Journal of the Mechanics and Physics of Solids*, 57(7):1093–1102, jul 2009.
 55. G. Carbone, M. Scaraggi, and U. Tartaglino. Adhesive contact of rough surfaces: Comparison between numerical calculations and analytical theories. *The European Physical Journal E*, 30(1):65–74, sep 2009.
 56. C. Putignano, L. Afferrante, G. Carbone, and G. Demelio. The influence of the statistical properties of self-affine surfaces in elastic contacts: A numerical investigation. *Journal of the Mechanics and Physics of Solids*, 60(5):973–982, may 2012.
 57. C. Putignano, L. Afferrante, G. Carbone, and G. Demelio. A new efficient numerical method for contact mechanics of rough surfaces. *International Journal of Solids and Structures*, 49(2):338–343, jan 2012.
 58. L. Afferrante, G. Carbone, and G. Demelio. Interacting and coalescing hertzian asperities: A new multiasperity contact model. *Wear*, 278-279:28–33, mar 2012.
 59. J A Greenwood. Constriction resistance and the real area of contact. *British Journal of Applied Physics*, 17(12):1621–1632, dec 1966.
 60. J. R. Barber. Bounds on the electrical resistance between contacting elastic rough bodies. *Proceedings of the Royal Society A: Mathematical, Physical and Engineering Sciences*, 459(2029):53–66, jan 2003.
 61. Wolf B. Dapp, Andreas Lücke, Bo N. J. Persson, and Martin H. Müser. Self-affine elastic contacts: Percolation and leakage. *Phys. Rev. Lett.*, 108(24):244301, jun 2012.
 62. Carlos Campaña. Using green’s function molecular dynamics to rationalize the success of asperity models when describing the contact between self-affine surfaces. *Physical Review E*, 78(2):026110, aug 2008.
 63. Lars Pastewka and Mark O. Robbins. Contact area of rough spheres: Large scale simulations and simple scaling laws. *Applied Physics Letters*, 108(22):221601, may 2016.
 64. Bo N. J. Persson. Contact mechanics for randomly rough surfaces: On the validity of the method of reduction of dimensionality. *Tribology Letters*, 58(1):58, mar 2015.
 65. Ian N. Sneddon. The relation between load and penetration in the axisymmetric boussinesq problem for a punch of arbitrary profile. *International Journal of Engineering Science*, 3(1):47–57, may 1965.
 66. I. A. Lyashenko, Lars Pastewka, and Bo N. J. Persson. On the validity of the method of reduction of dimensionality: Area of contact, average interfacial separation and contact stiffness. *Tribology Letters*, 52(2):223–229, aug 2013.